1. Report No.

PU-23-RP-05

2. Government Accession No

N/A

3. Recipient's Catalog No.

N/A

4. Title and Subtitle

Data-driven smart composite reinforcement for precast concrete

5. Report Date

December 2025

6. Performing Organization Code

N/A

7. Author(s)

Chengcheng Tao, Assistant Professor, 0000-0003-2708-0912
Shanyue Guan, Assistant Professor, 0000-0002-9358-0184
Yongfei Li, Yizhou Lin, Huaixiao Yan, Junyi Duan, Xiaoli Xiong, Sike Wang, Graduate Research Assistant

8. Performing Organization Report No.

PU-23-RP-05

9. Performing Organization Name and Address

Purdue University
363 N. Grant St., West Lafayette, IN 47907

10. Work Unit No.

N/A

11. Contract or Grant No.

69A3552348333

12. Sponsoring Organization Name and Address

Transportation Infrastructure Precast Innovation Center (TRANS-IPIC)
University of Illinois Urbana-Champaign.
Civil & Environmental Engineering.
205 N Mathews Ave, Urbana, IL 61801

US Department of Transportation
Office of Research, Development and Technology (RD&T)
1200 New Jersey Avenue, SE
Washington, DC 201590

13. Type of Report and Period Covered
Final Report
January 2024– November 2025

14. Sponsoring Agency Code

N/A

15. Supplementary Notes

For additional reports and information visit the TRANS-IPIC website https://trans-ipic.illinois.edu

16. Abstract
The work aims to establish an integrated framework that transforms the design process of reinforced precast concrete (PC) by combining sensing technology, experimental characterization, multivariate numerical modeling, and multi-objective metaheuristic optimization. Embedded smart self-sensed composite rebar and advanced testing provided comprehensive dataset on material behavior and interaction mechanisms within reinforced PC components. These experimental insights were paired with high-fidelity finite element analysis (FEA) capable of capturing the coupled mechanical response of the system. It was found that FEA can be effectively used to construct a large-scale simulation database for reinforced concrete beam design. A metaheuristic genetic algorithm optimization, coupled with a random forest surrogate model, was employed to search for optimal solutions that satisfy four objectives: maximizing load capacity while minimizing total cost, deflection, and damage ratio. The resulting non-dominated solutions on the Pareto front provide meaningful trade-offs among strength, cost, stiffness, and damage ratio. This study enables virtual design and optimization for reinforced concrete beams within a wide design space and provides an intelligent pathway to optimize the reinforced concrete system based on user-defined criteria.

17. Key Words

Precast concrete; optimization; finite element analysis; genetic algorithms; cracking

18. Distribution Statement

No restrictions.

19. Security Classification (of this report)	20. Security Classification (of this page)	21. No. of Pages	22. Price
Unclassified.	Unclassified.	30	N/A

Disclaimer:

The contents of this report reflect the views of the authors, who are responsible for the facts and the accuracy of the information presented herein. This document is disseminated in the interest of information exchange. The report is funded, partially or entirely, under 69A3552348333 from the U.S. Department of Transportation's University Transportation Centers Program. The U.S. Government assumes no liability for the contents or use thereof.

Transportation Infrastructure Precast Innovation Center (TRANS-IPIC)

University Transportation Center (UTC)

Data-driven smart composite reinforcement for precast concrete
[PU-23-RP-05]

FINAL REPORT

Submitted by:
PI: Chengcheng Tao, tao133@purdue.edu
Co-PI: Shanyue Guan, guansy@purdue.edu
School of Construction Management Technology
Purdue University

Collaborators / Partners:
North Dakota State University

Submitted to:
TRANS-IPIC UTC
University of Illinois Urbana-Champaign
Urbana, IL

Executive Summary:

It is critical to design high-performance, sustainable, and cost-effective reinforced precast concrete (PC) systems to extend the service life of transportation infrastructure and meet long-term societal needs. The design of reinforced PC components traditionally relies on extensive physical testing and iterative trial-and-error procedures, which demand substantial time, labor, and a large quantity of material. Such approaches make it difficult to efficiently explore the full range of reinforcement configurations, material combinations, and structural layouts required to achieve superior mechanical performance while also meeting economic constraints. As a result, there remains a significant gap in efficient and precise design pathways capable of simultaneously evaluating structural behavior and cost effectiveness across diverse design scenarios.

The research aims to establish an integrated framework that transforms the design process of reinforced PC by combining sensing technology, experimental characterization, multivariate numerical modeling, and multi-objective metaheuristic optimization. Embedded sensing and advanced testing provided comprehensive datasets on material behavior and interaction mechanisms within reinforced PC components. These experimental insights were paired with high-fidelity numerical simulations capable of capturing the coupled mechanical and economic responses of the system. Multi-objective optimization techniques, supported by Pareto front analysis, were applied to identify reinforcement strategies that achieve optimal performance across competing objectives:

<u>Task 1. Experimental investigation of mechanical properties of various reinforced PC components.</u> We investigated the mechanical performance of various reinforced PC components with different compositions, including PVA fiber inclusion, water content, beam span length, and rebar type. The sensor data and image data from the experiment were used to validate numerical models in Task 2 and generate database for AI-based condition assessment model in Task 3.

<u>Task 2. Multivariate numerical modeling of reinforced precast concrete components and physics-informed database establishment.</u> The task focuses on the development of three-dimensional (3D) finite element analysis and parametric study to analyze the sensitivity of various influencing factors on the mechanical properties of the reinforced concrete components. Multiple influencing factors will be considered, including the type of concrete materials, the effect of longitudinal rebars, the effect of fiber volume fraction, and the effect of rebar stirrups. The numerical analysis results were compared and validated by the experimental data in Task 1. As the complement of the data obtained from Task 1, the numerical data was integrated with fiber optical sensor data in Task 1 to establish a comprehensive physics-informed database for training AI algorithms in Task 3.

<u>Task 3. Development of multi-objective metaheuristic optimization framework with Pareto front analysis to achieve optimal mechanical properties and economic values.</u> This task focuses on developing a multi-objective optimization framework to efficiently provide optimal solutions for high-performance and low-cost reinforced precast concrete components.

Table of Contents

1. Problem description:

It is critical to design high-performance, sustainable, and cost-effective reinforced precast (PC) systems to extend the service life of transportation infrastructure and meet the increasing demands for structural reliability and environmental responsibility. Traditional design methods for reinforced PC components rely heavily on iterative physical testing and trial-and-error procedures, which consume significant time, labor, and a large quantity of material. These approaches make it challenging to efficiently explore the wide range of reinforcement configurations, material combinations, and performance requirements needed for optimized mechanical properties and economic feasibility. At present, there remains a lack of an integrated and precise framework that can simultaneously evaluate structural performance and cost efficiency while capturing the complex interactions between ingredients and the whole reinforced PC system.

2. Background:

Concrete is inherently brittle and shows low tensile strength relative to its compressive strength. To overcome this limitation, it is commonly combined with reinforcement (e.g., steel, composite) to form a synergistic structural system. Reinforced precast concrete is one of them and has been widely used in modern civil and infrastructure applications [1,2]. In the design of reinforced PC components, multiple strategies exist to enhance structural performance, namely increasing concrete strength, adopting fiber-reinforced polymer (FRP) rebars, or inclusion of fiber into the mix [3].

In addition, an accurate and real-time structural health monitoring system is essential for assessing the conditions of reinforced PC system. Conventional health monitoring system, such as direct visual inspection, are often impractical due to the inaccessibility of reinforcement. Moreover, destructive testing is an invasive, time-consuming evaluation approach. The strain gauge, though widely used, typically operates at a relatively high frequency to capture more data points within a given time frame. This high-frequency operation increases noise sensitivity and degrades data quality. Additionally, strain gauge only provides localized, point-based measurements, limiting its ability to capture strain distribution over a large area. In recent decades, distributed fiber optic sensing technology has greatly developed. Distributed fiber optic sensor (DFOS) operates based on the principle of light scatterings to measure strain distributions along the length of an optic fiber. When a short laser pulse is injected into one end of the fiber, a portion of the light is backscattered due to natural impurities and microscopic imperfections in the fiber core [4]. By analyzing variations in the backscattered signal, DFOS enables continuous, high-resolution monitoring of structural health condition. Furthermore, DFOS has advantages of being small in size and lightweight, allowing for easy installation on reinforcement surface for strain measurement [5]. Past studies have demonstrated the effectiveness of DFOS in monitoring reinforcement strain. Fan et al. [6] investigated the feasibility of DFOS in corrosion monitoring of steel reinforcement in reinforced concrete and found that it not only measured strain but also quantified corrosion-induced degradation. In addition to steel reinforcement, DFOS has also been applied to fiber FRP reinforcement. Creep and flexural tests on glass fiber reinforcement polymer (GFRP) PC beams showed that DFOS accurately measured longitudinal strain on the GFRP reinforcement [7]. The results also indicated that DFOS exhibited minimal sensitivity to temperature variations, making it ideal for use in harsh environment [8]. Given the small gauge length of DFOS, it enables precise strain measurement at closely spaced intervals, capturing localized strain variations [9]. This high-spatial-resolution measurement approach makes composite reinforcement with DFOS achieve “smart self-sensing”, facilitating sensitive crack detection and early damage identification.

Numerous studies have investigated the feasibility of DFOS in concrete structural components with FRP, such as basalt FRP-PC beam [10], carbon FRP sheet-strengthened concrete shear wall [11], and GFRP panel-strengthened concrete sewage pipe [12]. A commonality among these studies is highlighting the capability of DFOS for real-time SHM in the concrete structure with FRP by employing experimental approaches. However, experiment requires substantial time, labor, and material resources to real-time monitor structural and materials conditions and detect failure or anomalies in service. Moreover, most studies have focused on FRP-strengthened concrete structures, particularly those incorporating externally applied FRP sheets or layers. Given these limitations, developing an efficient and accurate approach for assessing composite PC structures is crucial.

Finite element analysis (FEA) presents an applicable solution to complement experimental method, providing a cost-effective and scalable way of evaluating structural performance. FEA allows for detailed modeling of the nonlinear behavior of both concrete and rebar, capturing critical aspects such as material degradation [13], cracking [14], and the interfacial bond-slip relationship [15] [16]. By complementing experimental findings, FEA enhances the understanding and prediction of structural performance in a reinforced concrete system. Through FEA simulations, it is possible to examine the cracking patterns, maximum loading, and deflection at the maximum loading point over different designs, with a focus on accurately defining the cracking path using tension damage (also known as DAMAGET) parameters. Seok et al. utilized the results of DAMAGET to represent the damage level associated with cracking [17]. As a result, the DAMAGET can serve as one of the concrete damage plasticity (CDP) model's outcomes.
Metaheuristic optimization algorithms have emerged as particularly effective tools due to their flexibility and robustness in solving complex, nonlinear optimization problems and in searching for optimal solutions in large databases [18]. Among various optimization algorithms, genetic algorithms (GA) have been widely used in structural design problems involving reinforced PC columns and beams. Notable early applications demonstrated the GA's capability in handling discrete variables, multi-objective functions, and practical design constraints [19–22]. With the continuous advancement of computational tools, programming languages, and modeling environments, the potential for more accurate and efficient analysis has increased.

However, identifying the optimal combination of these design variables is challenging due to the complex interaction among multiple performance objectives. To address this challenge, metaheuristic optimization offers a promising approach for exploring complex design spaces and determining the trade-off optimal solutions. Yet, the effectiveness of such optimization frameworks critically depends on the availability of large, diverse, and high-quality datasets. Generating such datasets solely through experimental testing is often time-consuming, costly, and logistically difficult. It is wise to leverage finite element analysis (FEA) to generate a big dataset across a wide range of design scenarios.

3. Research scope and objectives:

The research aims to establish an integrated framework that transforms the design process of reinforced PC by combining sensing technology, experimental characterization, multivariate numerical modeling, and multi-objective metaheuristic optimization. Embedded sensing and advanced testing provided comprehensive datasets on material behavior and interaction mechanisms within reinforced PC components. These experimental insights were paired with high-fidelity numerical simulations capable of capturing the coupled mechanical and economic responses of the system. Multi-objective optimization techniques, supported by Pareto front analysis, were applied to identify reinforcement strategies that achieve optimal performance. Research objectives are shown as follows.

<u>Objective 1. Conduct experimental investigation of mechanical properties of various reinforced PC components.</u> We investigated the mechanical performance of various reinforced PC components with different compositions, including Polyvinyl alcohol (PVA) fiber inclusion, water content, beam span length, and rebar type. The sensor data and image data from the experiment will be used to validate numerical models in Task 2 and generate database for AI-based condition assessment model in Task 3.

<u>Objective 2. Perform multivariate numerical modeling of reinforced precast concrete components and physics-informed database establishment.</u> The task focuses on the development of three-dimensional (3D) finite element analysis and parametric study to analyze the sensitivity of various influencing factors on the mechanical properties of the reinforced concrete components. Multiple influencing factors will be considered, including the type of concrete materials, the effect of longitudinal rebars, the effect of fiber volume fraction, and the effect of rebar stirrups. The numerical analysis results will be compared and validated by the experimental data in Task 1. As the complement of the data obtained from Task 1, the numerical data will be integrated with sensor data in Task 1 to establish a comprehensive physics-informed database for training AI algorithms in Task 3.

Objective 3. Develop multi-objective metaheuristic optimization framework with Pareto front analysis to achieve optimal mechanical properties and economic values. This task focuses on developing a multi-objective optimization framework to efficiently provide optimal solutions for high-performance and low-cost reinforced precast concrete components.

4. Research description:

4.1 Task 1: Experimental investigation of mechanical properties of various reinforced precast concrete components

Concrete is a brittle material and is prone to cracking. These cracks reduce the service life of reinforced PC because they facilitate chloride ingress and accelerate the corrosion of steel rebars. The usage of FRP rebar reinforcement can eliminate corrosion issues, and PVA fibers can mitigate cracking. On the other hand, monitoring reinforced concrete elements is important to ensure structural safety. In Task 1 systematically examines the mechanical behavior of PC components incorporating PVA fibers, various water contents, and different reinforcement types. The investigation integrates concrete workability, concrete compressive strength, flexural performance of reinforced beams, and validation using "smart self-sensors" and FEA. This multi-stage methodology provides a comprehensive understanding of how fiber dosage, water content, and rebar reinforcement influence structural performance. The experimental program began with slump testing, which established the workability of fiber-reinforced concrete mixtures. Commercial 5000 PSI dry concrete was proportioned with PVA fibers at 0.2%, 0.4%, and 0.6% by volume, while water content ranged from 87 to 113 mL/kg. Next, compressive strength testing was performed on cylindrical specimens (101.6 mm × 203.2 mm) cured for 28 days. The Forney FHS-400-VFD automatic compression test machine was used for both the compressive strength tests (with the compression loading configuration) and the center-point flexural tests (with the corresponding flexural loading configuration). To assess structural behavior, center-point flexural tests were conducted on reinforced PC beams with different configurations (with or without PVA fibers, rebar types and span length). Innovative distributed fiber-optic sensors (DFOS) were embedded along the reinforcement to enable real-time strain monitoring. Sensors were coated with DP460 epoxy for protection and bonding. Beams were air-cured and tested using a center-point flexural setup at a loading rate of 0.05 MPa/s. Finally, FEA model validation was performed using a quarter-model geometry with CDP to simulate material behavior. DFOS strain data (smoothed using a Savitzky–Golay filter) and crack patterns matched to FEA predictions at the different time moments. Overall, Task 1 effectively combines experimental testing and computational modeling to characterize and validate the mechanical performance of smart, fiber-reinforced precast concrete components.

4.2 Task 2: Multivariate numerical modeling of reinforced precast concrete components and physics-informed database establishment

Task 2 focuses on developing a comprehensive multivariate numerical framework to investigate the structural response of reinforced PC components under flexural loading and to establish a physics-informed database for subsequent optimization and machine-learning tasks. The research integrates FEA, parametric studies, sensitivity assessments, and large-scale automated simulations to capture the combined influence of concrete strength, fiber content, reinforcement type, and stirrup configuration. The investigation of sensitivity analysis begins with a detailed evaluation of concrete compressive strength effects. Using the Abaqus CDP model, reinforced concrete beams with compressive strengths of 35.8 MPa, 68.9 MPa, and 151.7 MPa are simulated under a vertical load of 52,800 N. Next, the effect of PVA fiber content was examined by modeling beams with 0%, 0.2%, 0.4%, and 0.6% fiber volume fractions. The effect of stirrups on structural behavior was also analyzed. Building on these parametric results, Task 2 then establishes a large physics-informed numerical database comprising 432 FEA cases with different parameter ranges. Each case represents a unique combination of key variables, including concrete strength (20.7–48.3 MPa), fiber content (0% or 0.66%), presence or absence of stirrups, and different rebar types (aramid FRP (AFRP), basalt FRP (BFRP), carbon FRP (CFRP), and glass FRP (GFRP) or various grades of steel). Automated Python scripts were developed to generate geometry, assign materials, mesh the models, and extract flexural performance outputs. All simulations were conducted using one-fourth models to reduce computational cost while preserving structural behavior. The completed database, supported by realistic material property ranges from literature and market-based cost data, provides a robust foundation for structural optimization, economic evaluation, and machine-learning-based predictive modeling in subsequent tasks.

4.3 Task 3: Development of a multi-objective metaheuristic optimization framework
Task 3 establishes a surrogate-assisted multi-objective optimization framework to identify the optimal design of reinforced precast concrete beams by balancing cost, structural capacity, deflection, and crack resistance. Using the 432 FEA simulations generated in Task 2, each beam configuration, defined by rebar type, concrete strength, stirrup condition, rebar area, and fiber content, is evaluated against four performance objectives: minimizing total cost, maximizing load capacity, minimizing mid-span deflection at yield, and minimizing surface tensile damage (DAMAGET). To efficiently search the high-dimensional design space, the framework integrates Random Forest regressors with a Genetic Algorithm (GA). Independent Random Forest models learn the nonlinear relationships among variables and predict objective values during optimization. A normalized aggregated fitness function is formulated to combine the four objectives. The GA is implemented using the Distributed Evolutionary Algorithms in Python (DEAP) package to handle nonlinear, multi-modal interactions. To interpret design trade-offs, the study constructs 3D Pareto fronts by removing one objective at a time and fitting smooth regression surfaces. These Pareto fronts reveal critical compromises between cost, strength, deflection, and damage, guiding engineers toward balanced and efficient beam designs under multiple competing constraints.

5. Project results:

5.1 Task 1: Experimental investigation of mechanical properties of various reinforced precast concrete components

5.1.1 Concrete Slump Test

Water content plays a critical role in concrete performance because it directly influences porosity, which governs mechanical strength and durability [23]. The addition of fibers can mitigate cracking and improve concrete ductility, but increasing fiber dosage often reduces workability [24]. To compensate, additional water is commonly introduced, which may lead to higher porosity and reduced compressive strength. Therefore, identifying the optimal water content for fiber-reinforced concrete is essential to balancing workability, strength, and crack resistance ability [25]. Slump tests, the most common method for assessing the workability of fresh concrete [26], are conducted to determine the appropriate water content for different fiber dosages. According to ACI 211 Section 6.3.1 [27], the recommended slump of concrete used as beams is 25.4–101.6 mm (1 to 4 in), which we follow in our design. Commercial 5000 PSI dry concrete mix by MASTERCRAFT was used. Lab tap water was used as mixing water. PVA fibers (13 mm in length) were used with volume fractions (0.2%, 0.4%, and 0.6%). After first mixing the dry concrete mix with mixing water, fiber was added and mixed for at least five minutes to ensure better dispersion. For clarity, the water content (mL) was expressed relative to the weight of the dry concrete mix (kg). Figure 1 shows the slump test results. It was found that slump decreases with increasing fiber content but improves with higher water content. For example, at 0.2% fiber content, slump increased from 10.2 mm to 152.4 mm as water content rose from 87 mL/kg to 100 mL/kg of dry concrete mix. Similar trends were observed at 0.4% and 0.6% fiber content.

(a) (b) (c) (d)

(e) (f) (g) (h)

Figure 1. Slump test results (a) 0.2% fiber with 87 mL/kg water; (b) 0.2% fiber with 100 mL/kg water; (c) 0.4% fiber with 87 mL/kg water; (d) 0.4% fiber with 100 mL/kg water; (e) 0.4% fiber with 113 mL/kg water; (f) 0.6% fiber with 87 mL/kg water; (g) 0.6% fiber with 100 mL/kg water; (h) 0.6% fiber with 113 mL/kg water.

5.1.2 Concrete Compressive Test

Compressive strength is a fundamental mechanical property of concrete. Concrete cylinders (101.6 mm in diameter and 203.2 mm in height) with various water contents and PVA fiber dosages were water cured for 28 days in the laboratory at 23 °C. The test used Forney FHS-400-VFD automatic compression test machine, with 2.0 kN preload and a ramp rate of 0.25 MPa/s. Figure 2 shows the 28 day compressive strength. It was found that at 0.2% fiber, compressive strength reached peak (41.4 MPa) at 87 mL/kg and decreased with increasing water content. At 0.4% fiber, peak strength (33.8 MPa) shows that the favorable water consumption is 100 mL/kg. Similarly, at 0.6% fiber, the compressive strength peaked at 34.7 MPa. So the message is clear that with increases in water content, the compressive strength first increases and then decreases. The increase is because is because concrete with fiber inclusion requires slightly more water to achieve better dispersion, while excessive water leads to increased porosity [28], and this negative effect dominates when water content is too high.

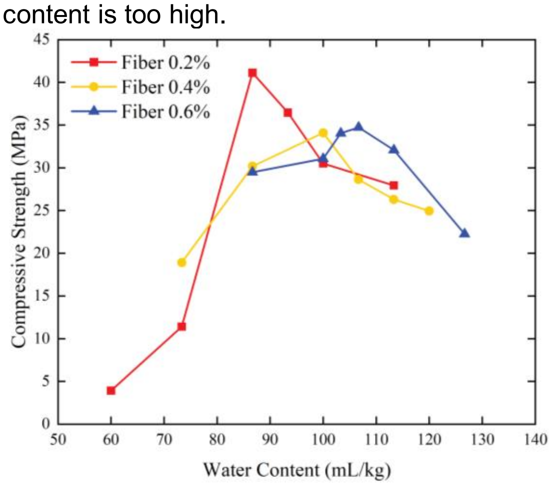

Figure 2. Compressive strength with different water and PVA fiber content.

Figure 3 illustrates the influence of fiber dosage on fracture behavior after compression. Figure 3 (a) shows the specimen with 0.2% fiber exhibits pronounced vertical cracks that extend continuously from top to bottom. The cracks are wide and linear, indicative of brittle failure with minimal energy dissipation. No visible fiber bridging is observed. Figure 3 (b) shows the cylinder with 0.4% fiber. The number of cracks increases, and the cracks become more closely spaced, indicating an improved energy dissipating ability. In Figure 3 (c), the specimen with 0.6% fiber exhibits a greater number of cracks but with smaller crack widths. The formation of more and finer cracks indicates improved durability as the chloride ingress pathways are controlled and significantly reduced [29]. Since the 0.6% fiber mixture with 107 mL/kg water exhibited the ideal strength and finer cracking pattern, it was selected for the flexural testing of fiber-incorporated beam. For the non-fiber beam, 87 mL/kg was selected.

(a) (b) (c)

Figure 3. Compression of failure modes of cylinder with various PVA fiber content: (a) 0.2%; (b) 0.4%; (c) 0.6%.

5.1.3 Reinforced Beam Center-Point Flexural Test Setup

Figure 4 (a) shows the schematic of the testbed for smart, self-sensing composite rebar in PC beam with various image capturing devices. To investigate the influence of PVA fiber inclusion, water content, span length, and the type of reinforcement (steel rebar and GFRP) on the flexural performance of reinforced PC beams, beam specimens with dimensions of 152.4 mm × 152.4 mm × 508.0 mm and 152.4 mm × 152.4 mm × 914.4 mm, were prepared, with “smart self-sensors” on the rebars (DFOS, LUNA). They have a diameter of 125 µm, high flexibility (allowing them to wrap around reinforcement), a long sensing range (up to 2 km per optical fiber), and good water resistance. DFOS enables real-time strain monitoring along the entire length of the fiber. We embed the DFOS along the bottom of the rebars. Since DFOS is vulnerable to shear forces, the sensors were protected with a coating of 3M DP460 two-component epoxy, as shown in Figure 4(b). This epoxy layer also acted as an adhesive to ensure strong bonding between the sensor and the rebar, while tape was used to cover the sections where epoxy could not be applied, as illustrated in Figure 4(c). Figure 5 shows the beam preparation process and the test setup. The beam was air-cured under laboratory environment. The center-point flexural test of reinforced PC beam was then performed at given curing ages. The Forney FHS-400-VFD automatic compression test machine with center-point flexural loading configuration was used, with a ramp rate of 0.05 MPa/s[30]. The modulus of rupture can be calculated using $R=3PL/2bd^2$ as per ASTM C293 [31]. The span length was 457.2 mm for 508.0 mm length beam, and 762.0 mm for the 914.4 mm beam. From the optimal results of the compressive test, the concrete with 0.6% fiber by volume is mixed with 107 mL/kg water and the non-fiber beam mixed with 87 mL/kg water. Six beams were tested in total with five beams cured for around one month, and one beam cured for 66 hours in the lab.

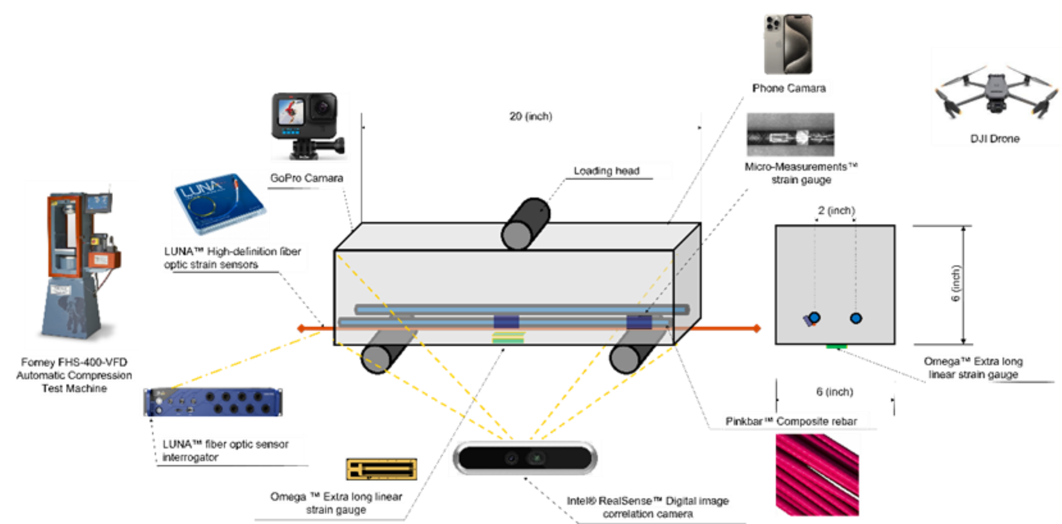

(a)

(b) (c)

Figure 4. Sensor embedment on rebar: (a) The schematic of the experimental setup of the smart composite reinforced concrete system. (b) applying epoxy on fiber optic sensor and rebar; (c) rebar after applying epoxy and tape.

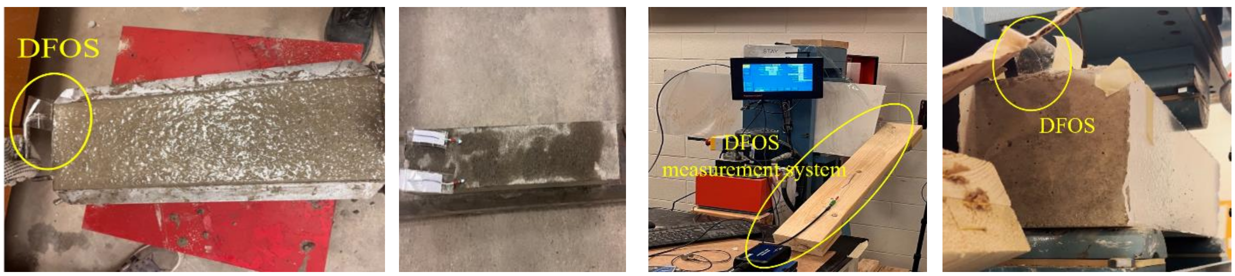

(a) (b) (c) (d)

Figure 5. (a) Freshly casted beam; (b) Demolded beam; (c) & (d) Center-point bending test setup.

5.1.4 Load versus Time Results of Center-Point Flexural Test

Figure 6 shows the load verses time results from center-point flexural test. As shown in Figure 6 (a), PVA fibers significantly reduces the modulus of rupture. For example, in the case of beams reinforced with steel rebar, the modulus of rupture decreases from 16.82 MPa (no fiber) to 13.93 MPa (0.6% fiber). It can be seen in Figure 6 (a) to (d), all beams containing fibers exhibit improved post-peak load-bearing capacity. This post-peak bearing phenomenon has also been reported in the literature for fiber reinforced concrete [32]. This behavior enhances the damage tolerance of the beam, thereby improving the overall structural safety [33]. In contrast, the load versus time curve for beams without fibers drops abruptly after reaching the peak load. The effect of fiber on strength is more obvious in beams reinforced with GFRP. The one-month GFRP reinforced beam with fibers exhibits an even lower modulus of rupture than the 66-hour beam without fibers. In addition, the beam with steel rebar has a higher modulus of rupture (13.93 MPa) than one with GFRP (10.81 MPa). This may be attributed to the weak bonding between GFRP bars and the surrounding concrete [34]. Furthermore, we observe that beams tested with a longer span length (508.0 mm) exhibit more fluctuations (“bumps”) in the load versus time curve during ramp up, indicating that more cracks are initiated prior to rupture. According to the experimental results, adding 0.6% fibers significantly enhances the energy dissipating ability of reinforced PC beams. In addition, steel rebars still outperformed GFRP in reinforced PC beam under center-point bending.

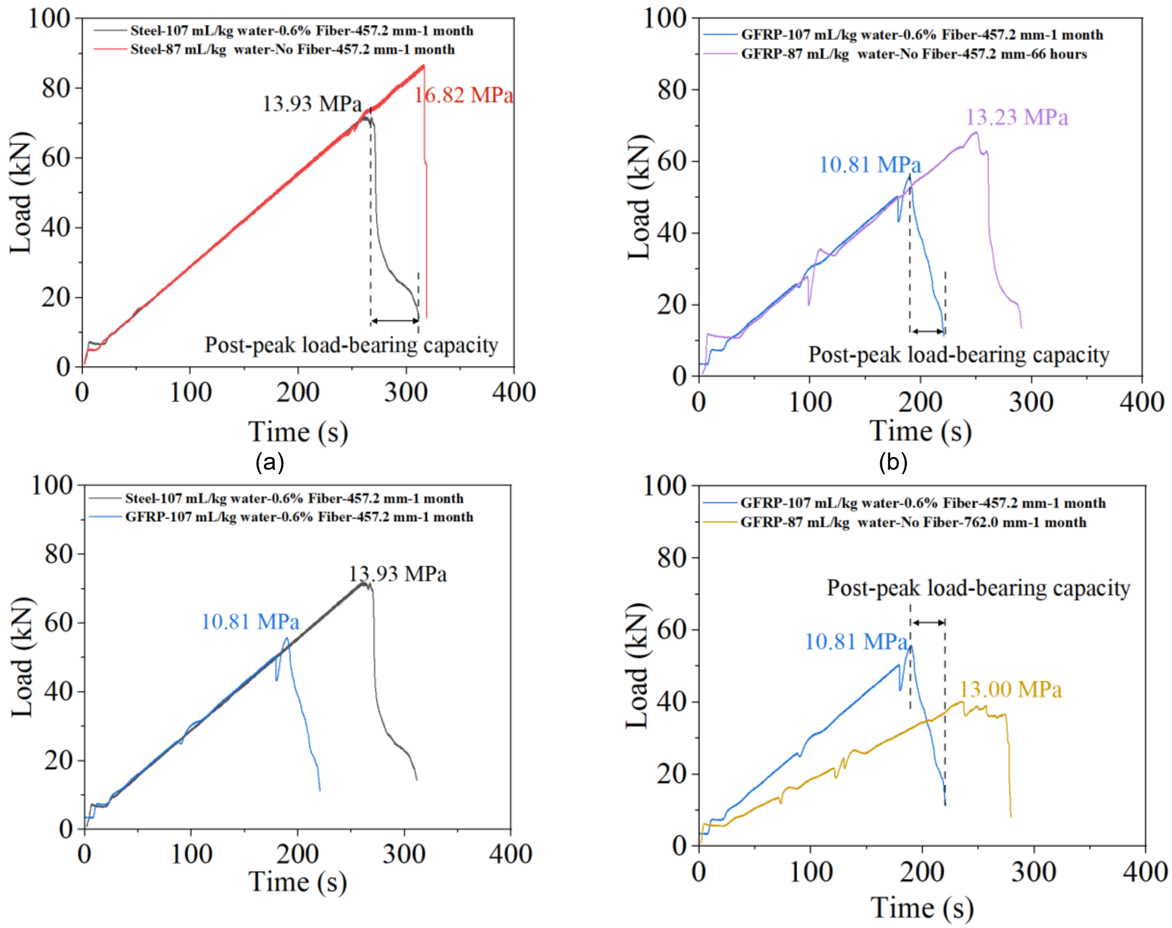

(c) (d)

Figure 6. Load verses time results: (a) Effect of inclusion of PVA fiber on beam with steel rebar; (b) Effect of inclusion of PVA fiber and curing age on beam with GFRP rebar; (c) Effect of GFRP and steel rebar on beam (d) Effect of span length and fiber inclusion on beam.

5.1.5 Results from Smart Self-Sensor and FEA Model Validation

Figure 7 shows the raw data and smoothed data from DFOS. The raw sensor readings vary along the length and include some noise and missing values, which were caused by damage during casting and curing or by imperfect bonding between the sensor and the rebar surface. To reduce these local fluctuations, the experimental strain profile was smoothed using a Savitzky–Golay filter with a window length of 51 points and a polynomial order of 3. For each original data point $P_i\,(x_i,s_i)$, the filter looks at 51 nearby points (25 on each side) and fits a third-order polynomial to them. The strain value at the original location x_i is then replaced with the value predicted by this polynomial. This process removes high-frequency noise while keeping the overall strain pattern intact.

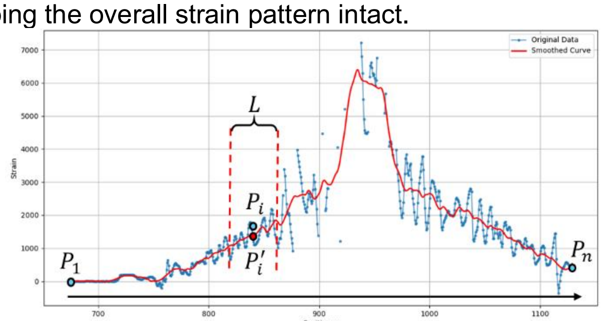

Figure 7. Raw strain data from DSOF and Savitzky–Golay smoothed strain data.

We also generated strain distribution from FEA and used the DFOS data for validation. To ensure consistency between numerical modeling and laboratory testing, the FEA was configured to replicate the same boundary conditions and loading protocols used in the experiments, as shown in Figure 8. The beam geometries in the simulations matched the experimental specimen sizes (152.4 mm × 152.4 mm × 508.0 mm and 152.4 mm × 152.4 mm × 914.4 mm), with span lengths of 457.2 mm and 762.0 mm, respectively. The load was applied at midspan through a load-controlled ramping procedure mimicking a physical center-point flexural test setup. The CDP model was used to simulate the concrete reinforced model.

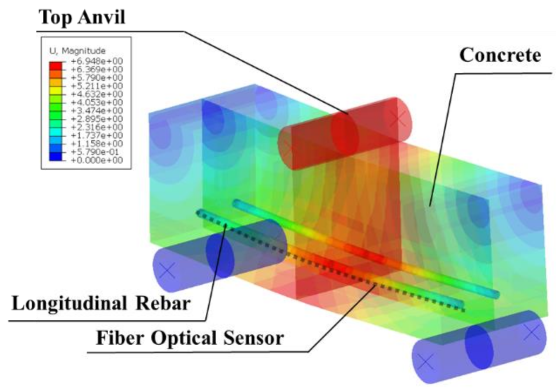

Figure 8. FEA validation model of center-point flexural test with rebar and embedded fiber optical sensor.

To keep the units consistent, the FEA strain values are converted to micro-strain. Figure 9 outlines the overall process used to compare the two sources of strain data. Because the DFOS records strain only as a function of time without directly capturing the applied load, and the FEA predicts strain based on actual loading values but does not represent real testing time, we use the time-load curve from the bending machine to link and calibrate the two datasets. Specifically, for each time point t_i, we identify the corresponding load from the compressive test machine record and use this load to query the FEA dataset and obtain the FEA strain at that moment, which forms the right-hand portion of the flow chart. At the same time point t_i is then converted to the actual timestamp (for example, 2025-09-13 18:33:08.171) by calculating its offset from the initial recorded time. Using this timestamp, the matching DFOS strain data is selected. Finally, the strain profiles along the beam length from both DFOS and FEA at each selected moment are produced and compared.

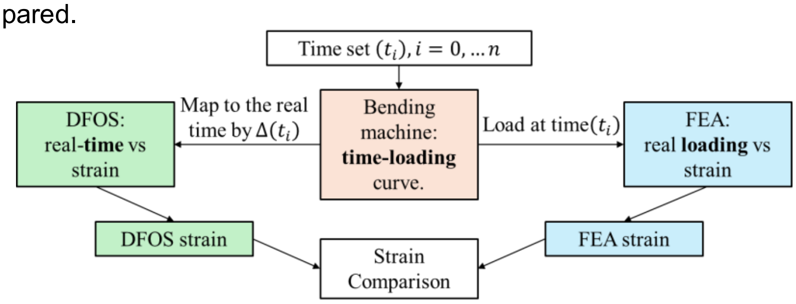

Figure 9. Flow chart of strain data comparison.

This comparison was performed in two dimensions: The spatial distribution of strain along the beam length and the temporal evolution of strain throughout the loading history. Figure 10 illustrates the strain profiles along the 457.2 mm span length at four distinct timestamps, representing different load levels during the experiment. In each sub-graph, the experimental data (depicted as the gray original data and the red smoothed curve) is compared directly with the theoretical predictions from the FEA model (blue FEA data). As the loading progresses from Figure 10 (a) to (d), the strain magnitude increases significantly. Despite local fluctuations in the raw sensor readings, the smoothed DFOS curve exhibits a strong correlation with the FEA strain distribution. Both datasets consistently show a parabolic-like strain profile, peaking at the mid-span and decreasing towards the supports. This agreement confirms the validity of the FEA in reproducing the global structural response.

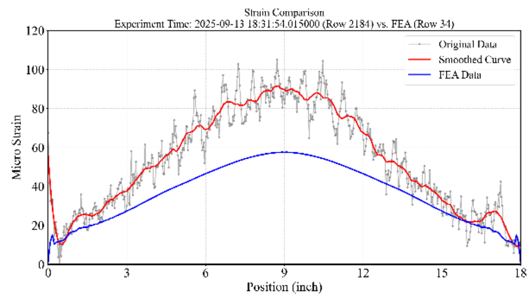

(a)

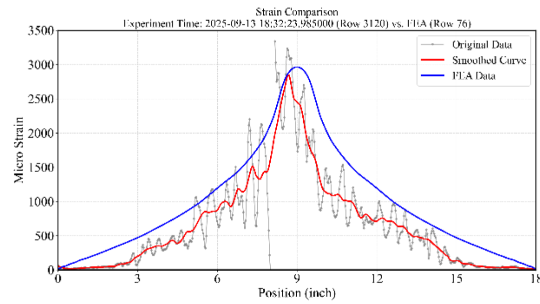

(b)

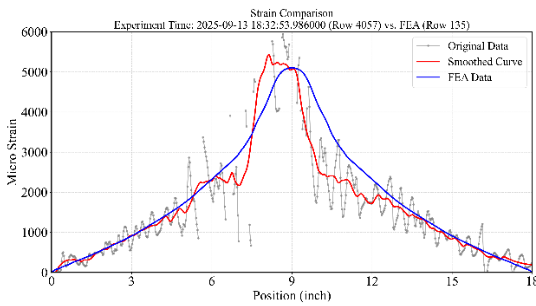

(c)

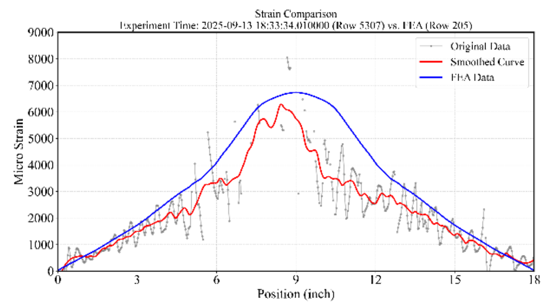

(d)

Figure 10. Strain data comparison at different timestamps.

To assess the sensor's performance over time, strain histories were extracted and compared at three specific critical locations. Figure 11 (a) details these monitoring points, located at distances of 57.2 mm (1/8 span), 114.3 mm (1/4 span), and 228.6 mm (1/2 span, center point) from the beam end. Figure 11 (b), (c), and (d) display the strain-time curves for these respective locations. The blue solid lines represent the experimental center strain recorded by the DFOS, while the red dashed lines represent the corresponding FEA predictions mapped to the experiment time. The comparison reveals that the sensor successfully tracks the strain evolution throughout the loading process. The experimental trends align well with the FEA predictions, capturing the gradual increase in strain as the load is applied. This consistency across the entire time domain validates the temporal reliability of the fiber optic sensor.

We also compare the crack patterns obtained from FEA with real crack propagations of experimental counterpart. Figure 12 shows the comparison results, demonstrating the accuracy of finite element models. In conclusion, the agreement observed in the spatial profiles (Figure 10), the temporal histories at key locations (Figure 11), and crack patterns (Figure 12), demonstrates that the reliable processed DFOS data and accurate numerical models. The sensor effectively captures both the localized strain gradients along the beam and the dynamic response over the duration of the test.

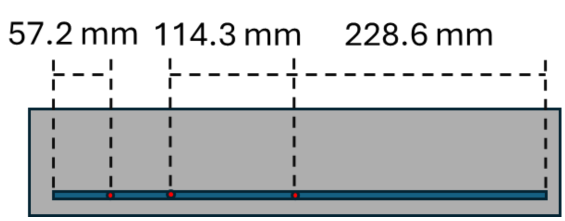

(a)

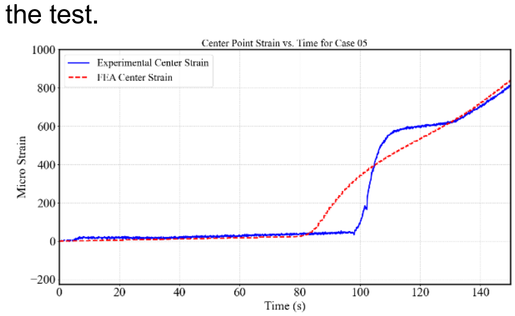

(b)

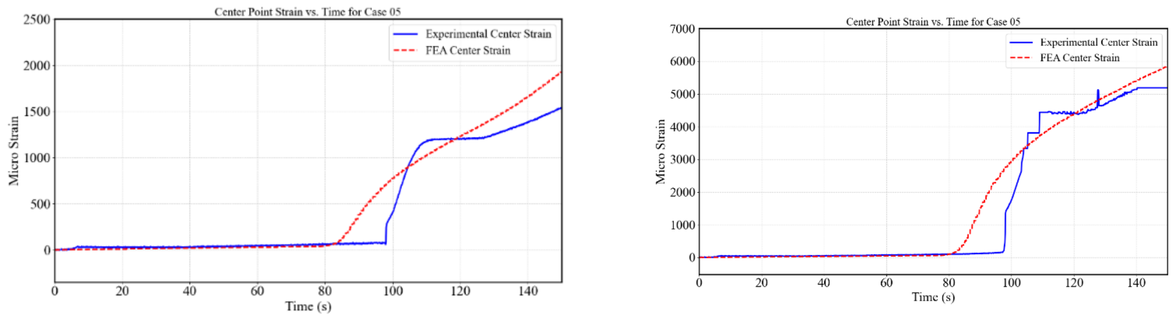

(c) (d)

Figure 11. Strain data comparison at some specific locations (a) Recorded points at 1/8, 1/4, and 1/2 span. (b) Strain comparison at 1/8 span. (c) Strain comparison at 1/4 span. (d) Strain comparison at 1/2 span.

The comparison of different contact interaction models reveals distinct outcomes in simulating the rebar strain distribution and concrete crack behavior in composite reinforced concrete systems. Figure 12 (b) illustrate that FEA prediction of the concrete damage pattern aligns closely with experimental crack propagation shown in Figure 12 (a).

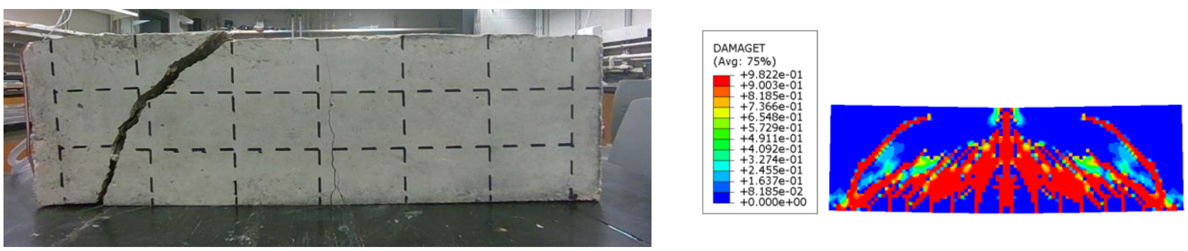

(a) (b)

Figure 12. Comparison of (a) real crack pattern from experiment and (b) numerical simulation crack patterns from FEA.

Overall, in Task 1, we successfully developed smart composite rebars in reinforced PC beams and demonstrated the real-time monitoring of composite rebars. The FEA predictions align well with the experimental results, showing the accuracy and reliability of our FEA model. The experiment results are integrated with the numerical results from Task 2 and used as input to train machine learning algorithms in Task 3.

5.2 Task 2: Multivariate numerical modeling of reinforced precast concrete components and physics-informed database establishment

5.2.1 Sensitivity Study

This section aims to investigate the effect of different parameters on the performance of the reinforced concrete beam through a sensitivity study. According to the sensitivity study results, the most important parameters will be selected and redefined in their ranges to generate a database in the 5.2.2 section.

5.2.1.1 Effect of Concrete Compressive Strength

Figure 13 presents FEA results for concrete beams with concrete compressive strengths of 35.8 MPa, 68.9 MPa, and 151.7 MPa subjected to a vertical load of 52,800 N. The 35.8 MPa concrete beam experienced extensive diagonal cracking and reached the highest yield stress distribution along the steel rebars, resulting in limited flexural resistance. In contrast, the 68.9 MPa beam exhibited much less cracking, primarily consisting of flexural cracks concentrated in the central region, with the highest stress in the steel rebar reaching 351 MPa. The highest-strength 151.7 MPa concrete beam demonstrated minimal damage, displaying only a single vertical flexural crack at the beam's mid-span. Due to the high strength of the concrete, the vertical displacement was minimal, measuring approximately 1.24 mm under the 52,800 N loading condition.

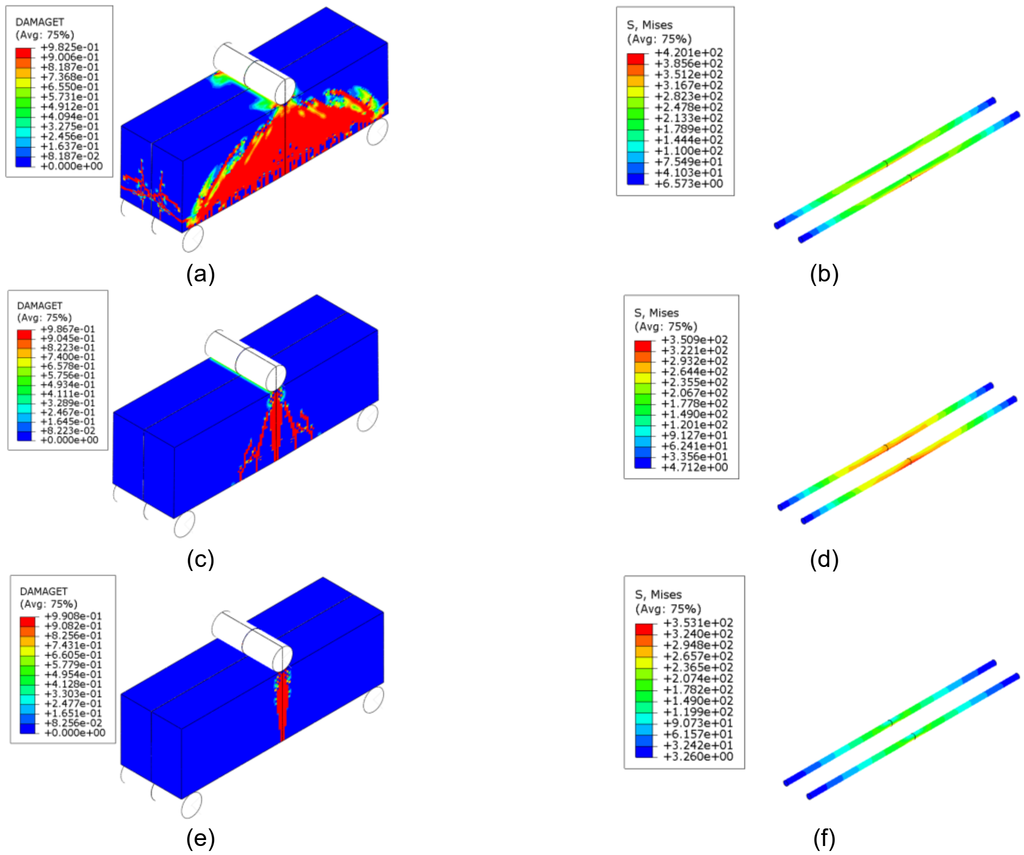

Figure 13. FEA results of compressive flexural beam simulations for 35.8 MPa, 68.9 MPa, and 151.7 MPa concrete under a load of 52,800 N: (a), (c), and (e) DamageT profiles for 35.8 MPa, 68.9 MPa, and 151.7 MPa concrete; (b), (d), and (f) Stress profiles of steel rebars for 35.8 MPa, 68.9 MPa, and 151.7 MPa concrete.

5.2.1.2 *Effect of Fiber Content*

This section mainly focuses on the performance of PVA fibers in reinforced concrete from the range 0% to range 0.6%. The influence of fiber content on concrete performance was also considered, as experimental evidence suggests a trade-off effect. Specifically, increasing the fiber volume fraction tends to reduce compressive strength, as observed in cylinder tests, but enhances tensile performance, as seen in split tensile tests. Similar trends have been reported in previous studies. For example, P. Zhang et al. found that when the volume fraction of PVA fibers increased to 1%, the cubic compressive strength dropped from 44 MPa to 39 MPa, while the tensile strength increased from 2.6 MPa to 3.05 MPa [35]. Thus, the compressive strength of concrete with fiber will be adjusted accordingly. Additionally, the simulation results revealed that vertical displacement decreases with increasing PVA fiber content, indicating improved overall strength. Under identical loading conditions, the beam without fibers exhibited the largest vertical displacement of approximately 2.20 mm. In comparison, the beam with a 0.2% fiber had a slightly reduced vertical displacement of about 1.94 mm. Beams with higher fiber contents showed further displacement reductions, approximately 1.73 mm for 0.4% fiber and 1.67 mm for 0.6% fiber. This displacement trend demonstrates that higher fiber volume fractions effectively reduce deformation and enhance the overall load-carrying capacity and stiffness of reinforced concrete beams.

Figure 14 illustrates a comparison between the simulations of concrete beams containing 0% and 0.6% fiber. The crack propagation patterns generally appear similar. The concrete beam containing fibers demonstrates less minor diagonal cracking in the middle region. The distribution of fibers bearing high stress closely corresponds to the damaged regions. As shown in Figure 14 (c), the highest stress in fibers, approximately 559.4 MPa, occurred near the bottom of the beam's central region.

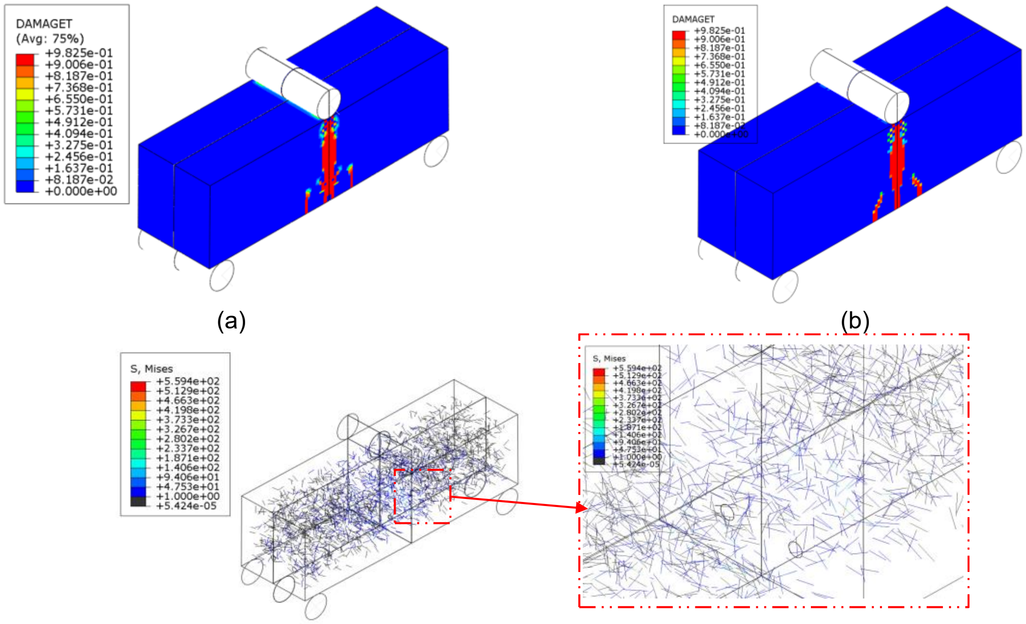

(a) (b)

(c)

Figure 14. FEA results of the compressive flexural beam simulation for 35.8 MPa concrete when the load reaches 28,512N: (a) DamageT profile for the beam without PVA, (b) DamageT profile for the beam with 0.6% fiber (c) PVA stress distribution for the beam with 0.6% fiber.

The damage profiles are shown in Figure 15 (a) and (b) indicate that the concrete beam with 0.2% fiber experienced more vertical cracking compared to the beam containing 0.4% fiber. Conversely, the beam with a 0.4% fiber exhibited more diagonal cracks, similar to the pattern observed in beams with a 0.6% fiber content. Furthermore, the stress distributions within the fibers in Figure 15 (c) and (d) reveal that the beam with 0.4% fiber reached a maximum fiber stress of 288.6 MPa, while the beam with 0.2% fiber reached a higher maximum fiber stress of 342.3 MPa. In conclusion, the FEA results demonstrate that varying volume fractions of PVA fibers enhance the flexural capacity of concrete beams reinforced with longitudinal G60 steel bars. The region of highest fiber stress for the 0.2%, 0.4%, and 0.6% fiber cases consistently occurred in the middle region of the concrete beams.

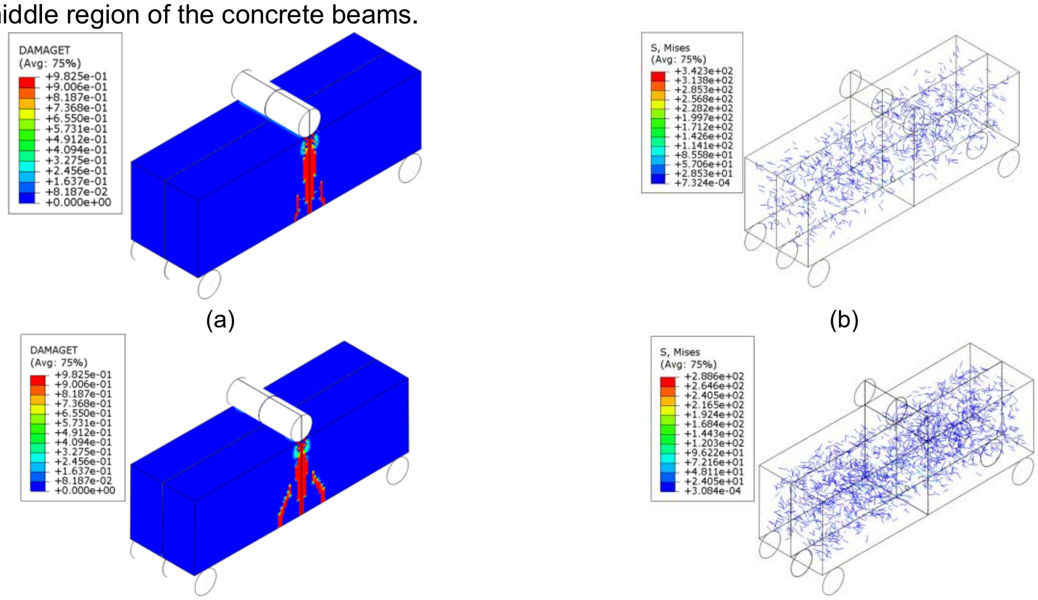

(a) (b)

(c) (d)

Figure 15. FEA results of the compressive flexural beam simulation for 35.8 MPa concrete when the load reaches 285kN: (a) DamageT profile for the beam with 0.2% fiber, (b) DamageT profile for the beam with 0.4% fiber, and PVA stress distribution for the beam with (c) 0.2% fiber and (d) 0.4% fiber.

5.2.1.3 Effect of Stirrups

This section mainly focuses on the performance of steel stirrups in reinforced concrete. The FEA results illustrate the behavior of concrete beams reinforced with longitudinal GFRP bars and steel stirrups at different concrete strengths. As shown in Figure 16, two flexural beam simulations are compared. The beam without steel stirrups exhibits a wider central flexural crack initiating from the bottom of the beam, while the beam reinforced with stirrups shows several vertical crack propagations concentrated in the middle region. Both models have additional crack propagation directly beneath the support area. Regarding vertical deflection, the reinforced beam with stirrups experiences a deflection of 1.61 mm, whereas the beam without stirrups deflects slightly more, at 1.79 mm. This corresponds to an approximate 10% reduction in deflection, which indicates that the added confinement increases the beam's overall stiffness. As a result, the beam can sustain higher loads before reaching the same deflection level, improving its load-carrying capacity.

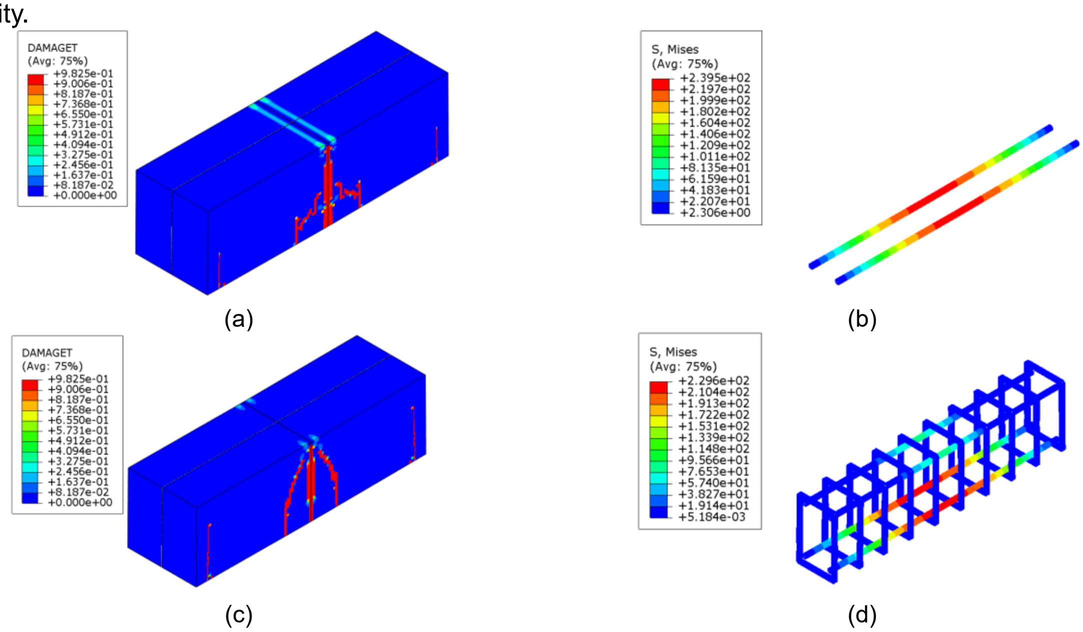

Figure 16. FEA results of the compressive flexural beam simulation for 35.8 MPa concrete with and without 9.5 mm stirrup when the load reaches 40 kN: (a) and (c) DamageT profile, (b) and (d) Rebar stress distribution.

<u>5.2.2 Database Generation</u>

Based on the sensitivity results, important parameters are selected as the design variables for the optimization. At previous sensitivity analysis stages, the exact extent of the concrete strength effect was not yet known, so using a broad span allowed us to establish clear trends. After a sensitive analysis, we found that the effect of concrete strength was too significant; thus, we decided to decrease the range, as other parameters can equally contribute to structural performance. This section discusses the generation of the validated database from FEA simulation, which consists of 432 cases developed to investigate the influence of various parameters on the structural behavior of reinforced concrete. The database was constructed using automated Python scripts to define geometry, assign materials, generate meshes, apply loading, and extract results. In the previous sensitivity analysis stages, the exact extent of the concrete strength effect and fiber effect was not yet known, so using a broad span allowed us to establish clear trends. After a sensitive analysis, we found that the effect of concrete strength was too significant; thus, we decided to decrease the range. Similarly to the fiber effect, we decided to increase the fiber range in the database generation. All cases in the database were loaded under displacement-controlled conditions, allowing for the accurate capture of the maximum loading force and the corresponding flexural displacement. Key variables were systematically varied, including rebar types (AFRP, BFRP, CFRP, GFRP, and steel rebars), rebar cross-sectional area, manufacturer or material specification, concrete strength (20.7, 34.5, and 48.3 MPa), presence of stirrups, and fiber volume fraction in concrete (0% and 0.66%).

Each simulation case models a reinforced concrete beam with dimensions of 152.4 mm × 152.4 mm × 508.0 mm. The model used one-fourth of the full-scale geometry to reduce computational cost. In configurations with stirrups, four longitudinal rebars are used, while cases without stirrups include only two rebars, which follow realistic practices. All stirrups are modeled using G60 steel with a 9.5 mm diameter. Figure 17 shows a general case of simulation geometry, including the concrete beam dimensions, rebar configuration, and variable parameters considered in the study. Simulations were executed using the CDP model with embedded contact under the static general step in Abaqus.

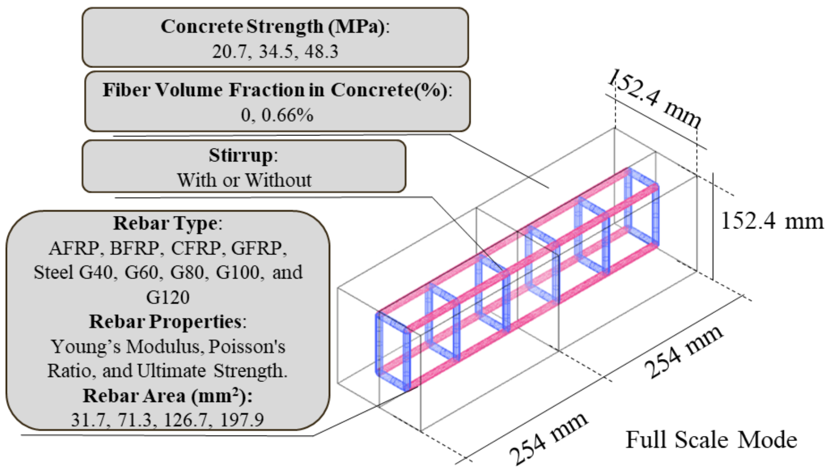

Figure 17. Geometric and parametric definition of the reinforced concrete beam used in FEA simulations.

The material properties used in the FEA simulations are presented in Table 1. It shows the corresponding values assigned to each material in the model. In this study, the mechanical properties of FRP materials were sourced from various literature references to reflect realistic behavior [36–47]. Based on information from all references, the mechanical properties required for the FEA models were defined and used to generate the full simulation database.

Table 1. List of Material Properties for a Composite Reinforced Concrete System [36–47].

Composite Rebar (from a different manufacturer) (AFRP: 1. General, 2. Arapree-8, 3. Technora; BFRP: 1. General, 2. Pultrusion, 3. Basalt-vinyl ester; CFRP: 1. General, 2, Leadline, 3. CFCC; GFRP: 1. Pink Bar, 2. General Sand-coated Pultrall Inc, 3. Quantum Company)	**Parameter**	**Lower Bound**	**Upper Bound**
	Composite rebar Young's modulus, E_r (GPa)	46.9	150
	Poisson's Ratio, n	0.3	0.3
	Composite rebar ultimate strength, $f_{u.r}$ (MPa)	728	3000
	Diameter, d (mm)	9.5	9.5
Steel Longitudinal Rebar / Stirrup (Steel G40 (longitudinal), Steel G60 (longitudinal/stirrup), Steel G80 (longitudinal), Steel G100 (longitudinal), Steel G120 (longitudinal))	Young's modulus, E_s (GPa)	200	200
	Poisson's Ratio, n	0.3	0.3
	Composite rebar ultimate strength, $f_{u.s}$(MPa)	480	1035
	Diameter, d (mm)	6.4	15.9
Concrete + PVA Fiber (**20.7 MPa+0, 0.66%, 34.5 MPa+0,0.66%, 48.3 MPa+0%, 0.66**%)	Concrete compressive strength, f'_c (MPa)	20.7	48.3
	Concrete tensile strength, f'_t (MPa)	3.0	4.23
	Concrete Young's modulus, E_c (GPa)	21.4	32.0

Table 2 illustrates the basic information and key parameters included in the FEA database. Each row corresponds to a unique reinforced concrete beam sample generated in FEA based on a specific combination of design variables, such as rebar type and area, concrete strength, stirrup (with or without), and fiber volume fraction in the concrete. Due to the large number of simulations, only the first seven cases and the final few entries are listed here for illustrative purposes.

Table 2. Summary of Simulation Cases and Parameter Combinations in the FEA Database

No.	Rebar Type	Rebar Diameter (mm)	Concrete Strength (MPa)	Stirrup	Stirrup Area (mm^2)	Stirrup Grade	Fiber Volume Fraction (%)
1	Steel G40	6.4	20.7	With	71.3	Grade 60	0%
2	Steel G40	6.4	20.7	With	71.3	Grade 60	0.66%
3	Steel G60	6.4	20.7	With	71.3	Grade 60	0%
4	Steel G60	6.4	20.7	With	71.3	Grade 60	0.66%
5	Steel G80	6.4	34.5	With	71.3	Grade 60	0%
6	Steel G80	6.4	34.5	With	71.3	Grade 60	0.66%
7	Steel G80	6.4	34.5	With	71.3	Grade 60	0%
………… (continued)							
431	GFRP	15.9	48.3	Without	71.3	Grade 60	0%
432	GFRP	15.9	48.3	Without	71.3	Grade 60	0.66%

To support the cost analysis within the database, typical market prices for all relevant materials were reviewed. For steel rebar, costs range from approximately \$1.21/kg for Grade 40 to \$2.32/kg for Grade 120, increasing with yield strength [36]. For FRP rebars, typical prices are approximately \$1/lb for GFRP, \$1.5/lb for BFRP, \$3/lb for AFRP, and \$6/lb for CFRP [48–50]. Concrete prices vary by strength level, with typical values ranging from \$174/m³ for 20.7 MPa mixes to \$218/m³ for 40.3 MPa mixes [51]. Additionally, incorporating fiber adds an extra cost of approximately \$5,160/m³ with pure fiber ingredient [52].

5.3 Task 3: Development of a multi-objective metaheuristic optimization framework

The structural optimization of reinforced concrete beams is a critical problem in civil engineering, as designers must balance cost efficiency, load-bearing capacity, and cracking resistance. Beam designs are simulated in Abaqus under center-point bending, with parameters systematically varied: nine rebar types, four bar sizes, three concrete strengths, stirrup inclusion (0/1), and fiber content. This produced 432 FEA cases for optimization. Each design is evaluated against four objectives: minimize the total beam cost, maximize the yield load capacity, minimize the mid-span deflection at yield load (Deflection in short), and minimize the surface tensile damage ratio. To search the design space efficiently, a surrogate-assisted framework combining Random Forest regressors with a Genetic Algorithm (GA) is used. Independent Random Forest models, each with 100 trees, captured nonlinear interactions and provided accurate predictions for the optimization process. The optimization problem is formulated as a single aggregated fitness function, balancing the four normalized objectives with weights.

$$Fitness = w_1 \times Cost + w_2 \times (1 - Load\ Capacity) + w_3 \times |Deflection| + w_4 \times Damage\ Ratio \quad (1)$$

where $w_1 + w_2 + w_3 + w_4 = 1$. The normalization ensures comparability between different scales: minimization objectives (unit cost, deflection, damage ratio) are scaled directly; maximization objective (yield load capacity) is inverted before normalization; and the absolute value of deflection is considered to enforce serviceability limits. The GA is implemented using Distributed Evolutionary Algorithms in Python (DEAP) framework, considering its ability to handle nonlinear, mixed-variable, multi-modal search space. Each candidate design is represented by six decision variables. Surrogate models predict objective values, aggregated into a scalar fitness score. As shown in Figure 18, fitness drops sharply in the first 5 generations before stabilizing, indicating rapid convergence.

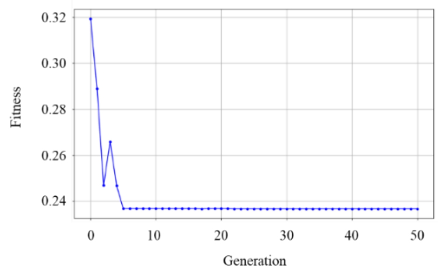

Figure 18. Convergence history of the GA.

No major improvement occurs after 10 generations, suggesting a stable optimum is achieved. The GA thus effectively explores the design space and identifies optimal beam parameters under equal weighting. The GA refined the population toward optimal trade-offs among cost, strength, stiffness, and damage resistance. To analyze these trade-offs, 3D Pareto fronts are generated by excluding one objective and optimizing the remaining three. Random forest surrogate models provided predictions, and Ridge regression surfaces are fitted post hoc to Pareto-optimal points for smooth visualization. This strategy clarifies interactions among objectives and shows how trade-offs shift when one metric is removed. Figure 19 displays the Pareto fronts of four optimization cases, with blue markers as optimal solutions, gray dots as raw data, and smoothed surfaces highlighting trade-off structures. Figure 19 (a) highlights the dominant compromise between economy and serviceability when the damage ratio is not explicitly constrained. Figure 19 (b) shows both deflection and damage improve until a threshold, after which further deflection reduction yields little damage benefit. The front on Figure 19 (c) forms a smooth ridge, indicating that without budget constraints, performance improves across all metrics. Figure 19 (d) shows a knee at cost 6-12 per unit, load 65-75 kN, and damage 0.007-0.013. Below this, cost cuts add little; above 75 kN, strength gains raise cost and damage. This balance preserves strength and damage ratio at a moderate cost.

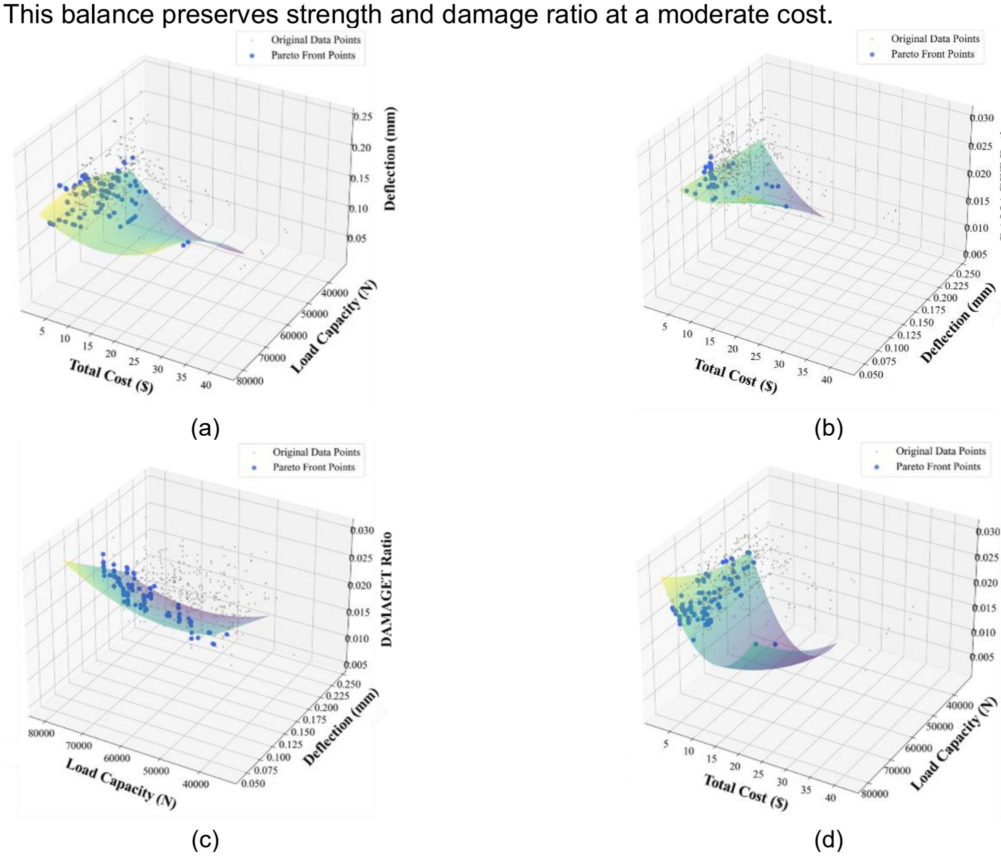

Figure 19. Pareto front of different multi-objective optimization cases: (a) min cost – max load capacity – min deflection; (b) min cost – min deflection – min damage ratio; (c) max load capacity – min deflection – min damage ratio; (d) min cost – max load capacity – min damage ratio.

6. Conclusions and recommendations:

This report presents a integrated experimental, numerical, and AI-assisted framework for analyzing and optimizing the performance of reinforced precast concrete components. The proposed approach demonstrates a scalable and data-driven pathway for achieving efficient and reliable beam designs across a broad range of structural configurations. By integrating laboratory testing, FEA simulations, and advanced metaheuristic optimization techniques, the study establishes an intelligent design methodology capable of supporting both performance evaluation and decision-making. This framework offers a versatile tool for optimizing reinforced concrete systems according to user-defined objectives such as cost, strength, serviceability, and durability. The main conclusions of the work are summarized as follows:

- Experimental results show that incorporating fibers requires additional mixing water to maintain workability, which can reduce the compressive strength of concrete and the modulus of rupture of reinforced PC beams. However, adding 0.6% PVA fiber (by volume) significantly increases the energy dissipating capability of the reinforced PC beam. Beams with steel rebars still outperform ones with GFRP in center-point flexural test. In addition, the FEA-predicted strain data and crack pattern agree well with the experimental measurements, providing a solid foundation for the developed multi-objective metaheuristic optimization framework.
- A validated database of 432 FEA cases was developed to capture how key design variables influence reinforced concrete beam performance. Sensitivity analysis guided refinement of parameter ranges, narrowing the concrete strength span and expanding the fiber content to ensure balanced effects across variables. Automated Python scripts generated all models, geometry, materials, meshing, loading, and result extraction under consistent displacement-controlled conditions. The database includes multiple FRP and steel rebar types, manufacturing types of FRP and steel rebars, varying rebar sizes, presence of stirrups, concrete strengths, and fiber contents. Material properties were sourced from literature, and market pricing data for steel, FRP, concrete, and fibers were integrated to support later cost–performance optimization. This comprehensive dataset provides the foundation for the multi-objective optimization framework.
- A surrogate-assisted multi-objective optimization framework was successfully applied, integrating Random Forest regressors with GA, to identify optimal designs for reinforced precast concrete beams. By leveraging 432 FEA simulation cases, the framework simultaneously addressed four competing objectives: minimizing total cost, deflection, and surface damage, while maximizing yield load capacity. The optimization process demonstrated high efficiency, achieving convergence and stabilizing within just 10 generations. Additionally, the analysis of 3D Pareto fronts visualized critical trade-offs, identifying a specific region that secures high strength and damage resistance at a moderate cost. Ultimately, this framework effectively navigates the non-linear design space, providing engineers with a robust tool for achieving balanced, cost-efficient structural performance.

Based on our findings, future work includes the investigation the long-term benefits of using non-corrosive FRP rebars, particularly with respect to durability, service life, and life cycle assessment. In addition, in FEA simulation, a major challenge is that each CDP model is highly demanding, consuming substantial computing resources while producing only a single data point for the Pareto front. Therefore, future research should focus on maximizing the utility of each simulation. Alternatively, one potential solution is to develop theoretical formulations based on ACI standards, allowing generalized predictions and generating additional Pareto front points without running every FEA case. While the current study focuses on the center-point bending, the framework can be extended to other loading conditions or more complicated structural geometries. In addition, further study includes the selection of appropriate weight factors for the various optimization objectives plays a critical role in maintaining the convergence stability of the Genetic Algorithm and in avoiding biased or skewed optimization outcomes.

7. Practical application/impact on transportation infrastructure:

In practical transportation applications, the experimental beam can serve as a representative prism of a slab or pavement, allowing the structural response of the full system to be inferred from prism-level analysis. This section provides an application example to illustrate how beam-scale modeling can be applied to pavement design. This schematic in Figure 20 is adapted from the Federal Highway Administration's analytical modeling approach for continuously reinforced concrete pavements, where a representative reinforced concrete prism with a centrally embedded rebar. Building on this concept, the prism methodology from the experimental beam tests and the accompanying simulation database was extended to the context of precast concrete pavements (PCP) [53]. In PCP design, a representative prism can be extracted from a panel and analyzed under a 4000 lb axle load of a design truck to capture the local stress response [54]. This approach avoids the need to model the entire panel while still reflecting its structural behavior. Within this database, parameters were varied by adjusting the rebar size at the prism center and by changing the rebar material, resulting in a dataset of 25 cases. By varying design parameters, a range of design scenarios can be explored to achieve an optimal balance between structural performance and cost efficiency for overall pavement systems.

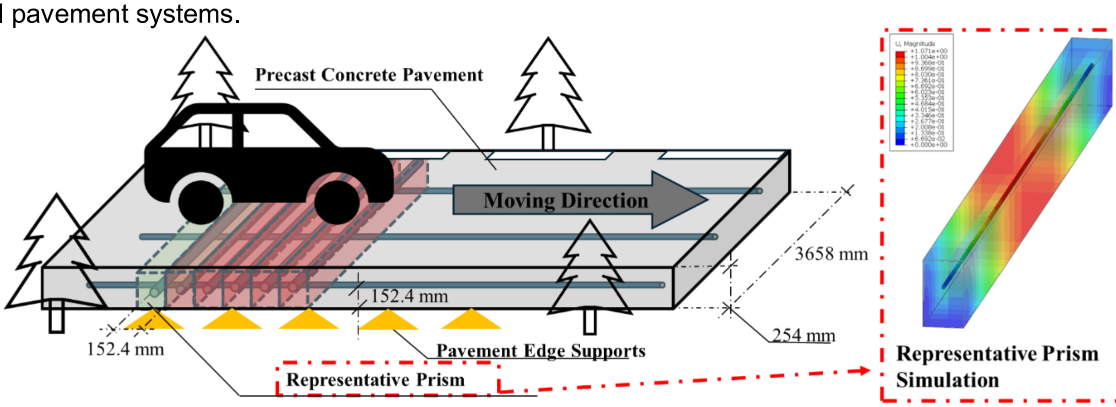

Figure 20. Schematic of a representative reinforced concrete prism for road pavement analysis.

An optimization framework is also developed to evaluate design alternatives for this prism structural element. The analysis considers two key design variables: the rebar material placed at the prism center, including steel rebar, Aramid Fiber Reinforced Polymer (AFRP), Basalt Fiber Reinforced Polymer (BFRP), Carbon Fiber Reinforced Polymer (CFRP), and Glass Fiber Reinforced Polymer (GFRP), with five different cross-sectional geometries (129, 200, 283.9, 387.1 and 509.7 mm^2), producing a dataset of 25 design cases. The aim is to simultaneously minimize total cost and mid-span deflection. Figure 21 shows the Pareto front to identify the non-dominated designs. As illustrated in the resulting Pareto plot, the optimal solutions mainly involve steel rebar. This outcome is consistent with structural mechanics expectations, as steel offers high stiffness at a comparatively low cost, giving it a natural advantage when only structural performance and initial cost are considered. However, composite rebars possess benefits that are not reflected in this simplified two-objective analysis, particularly durability, corrosion resistance, and long-term maintenance savings. Future work will therefore incorporate life-cycle assessment and additional sustainability metrics to more comprehensively evaluate the potential advantages of composite rebar materials.

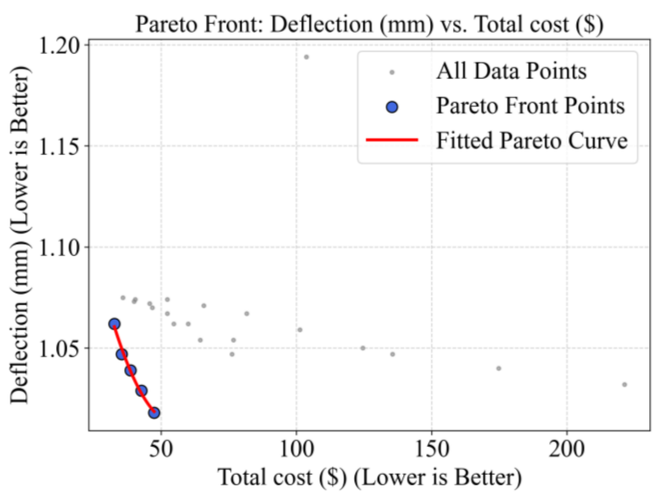

Figure 21. Optimized design for prism structures.

Figure 22 illustrates a bridge girder subjected to standard AASHTO HL-93 design loading . The HL-93 truck, a three-axle design vehicle under the same axle loads as in the previous pavement condition, represents the critical live load condition considered in bridge design. In addition to the live load at 9.3 kN/m, the design also incorporates dead load components, including the structural self-weight at 21kN/m and superimposed dead load at 10 kN/m. Together, these load cases reflect the comprehensive load combination used in AASHTO bridge design specifications. To improve the design of bridge girders under roadway loading conditions, a 25-case simulation database is developed. The database varies the size and material properties of the longitudinal rebar to identify an optimal balance between safety and economy while satisfying design safety requirements.

The developed AI-driven smart composite rebar provides continuous strain monitoring results along the entire length of the bridge girder, enabling the detection of localized strain peaks associated with crack formation. By identifying these distinct strain signals, the location and severity of cracks can be accurately determined. Furthermore, FEA is employed to correlate the strain results and provide a visualization representation of structural behavior through the digital twin model, as well as a physics-informed database for optimal design of the transportation infrastructure.

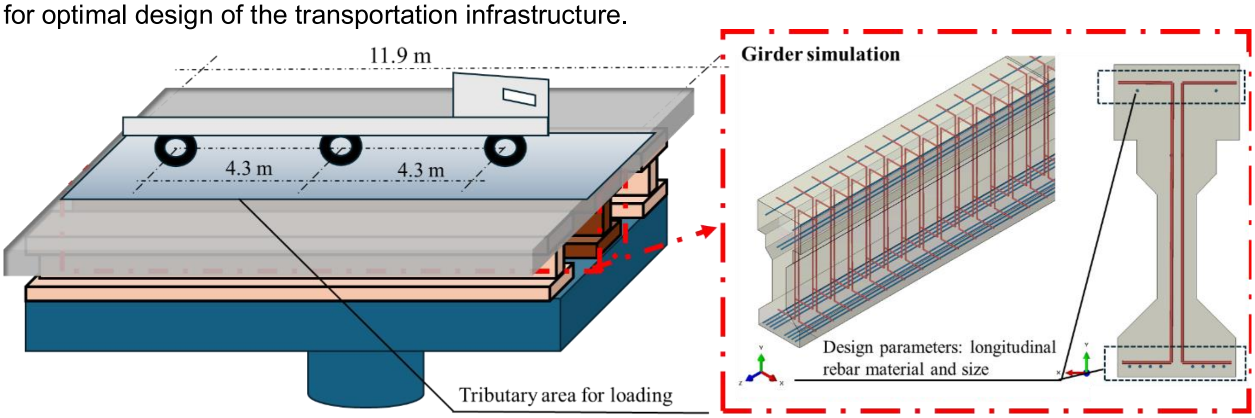

Figure 22. Bridge girder simulation framework with variable longitudinal rebar parameters.

8. References:

[1] X. Zhang, Q. Lu, Y. Wang, X. Zhang, Q. Lu, Y. Wang, Experimental Study on Bond Behavior between Steel Rebar and PVA Fiber-Reinforced Concrete, Coatings 13 (2023). https://doi.org/10.3390/coatings13040740.

[2] E.D. Reis, R.C. de Azevedo, A.L. Christoforo, F.S.J. Poggiali, A.C.S. Bezerra, Bonding of steel bars in concrete: A systematic review of the literature, Structures 49 (2023) 508–519. https://doi.org/10.1016/j.istruc.2023.01.141.

[3] V. Afroughsabet, L. Biolzi, T. Ozbakkaloglu, High-performance fiber-reinforced concrete: a review, J. Mater. Sci. 51 (2016) 6517–6551. https://doi.org/10.1007/s10853-016-9917-4.

[4] L. Strasser, W. Lienhart, M. Winkler, Static and dynamic bridge monitoring with distributed fiber optic sensing, Struct. Health Monit. 2023 (2023). https://dpi-proceedings.com.destechpub.a2hosted.com/index.php/shm2023/article/view/36932 (accessed January 29, 2025).

[5] J. Zhou, C. Kang, M. Peng, M. Stümpel, S. Marx, Investigations on bond performances of GFRP/stainless steel reinforcements using distributed fiber optical sensors (DFOSs), J. Build. Eng. 75 (2023) 106881.

[6] L. Fan, Y. Bao, G. Chen, Feasibility of distributed fiber optic sensor for corrosion monitoring of steel bars in reinforced concrete, Sensors 18 (2018) 3722.

[7] A. Kalamkarov, G. Saha, S. Rokkam, J. Newhook, A. Georgiades, Strain and deformation monitoring in infrastructure using embedded smart FRP reinforcements, Compos. Part B Eng. 36 (2005) 455–467.

[8] A. Singhvi, A. Mirmiran, Creep and Durability of Environmentally Conditioned FRP-RC Beams Using Fiber Optic Sensors, J. Reinf. Plast. Compos. 21 (2002) 351–373. https://doi.org/10.1177/0731684402021004254.

[9] Y. Lemcherreq, T. Galkovski, J. Mata-Falcón, W. Kaufmann, Application of distributed fibre optical sensing in reinforced concrete elements subjected to monotonic and cyclic loading, Sensors 22 (2022) 2023.
[10] Y. Tang, Z. Wu, Distributed long-gauge optical fiber sensors based self-sensing FRP bar for concrete structure, Sensors 16 (2016) 286.
[11] J.E. Woods, D.T. Lau, X. Bao, W. Li, Measuring strain fields in FRP strengthened RC shear walls using a distributed fiber optic sensor, Eng. Struct. 152 (2017) 359–369.
[12] P. Popielski, B. Bednarz, R. Sieńko, T. Howiacki, Ł. Bednarski, B. Zaborski, Monitoring of large diameter sewage collector strengthened with glass-fiber reinforced plastic (GRP) panels by means of distributed fiber optic sensors (DFOS), Sensors 21 (2021) 6607.
[13] M. Qasem, M. Hasan, R. Muhamad, C.-L. Chin, N. Alanazi, Generalised calibration and optimization of concrete damage plasticity model for finite element simulation of cracked reinforced concrete structures, Results Eng. 25 (2025) 103905. https://doi.org/10.1016/j.rineng.2024.103905.
[14] E. Korec, M. Jirásek, H.S. Wong, E. Martínez-Pañeda, A phase-field chemo-mechanical model for corrosion-induced cracking in reinforced concrete, Constr. Build. Mater. 393 (2023) 131964. https://doi.org/10.1016/j.conbuildmat.2023.131964.
[15] R. Jakubovskis, G. Kaklauskas, Damage of bond in reinforced concrete: A detailed finite element analysis, Struct. Concr. 22 (2021) 3228–3240. https://doi.org/10.1002/suco.202100229.
[16] F. Chen, Z. Yu, Y. Yu, Q. Liu, Study on the bond-slip numerical simulation in the analysis of reinforced concrete wall-beam-slab joint under cyclic loading, Constr. Build. Mater. 449 (2024) 138266. https://doi.org/10.1016/j.conbuildmat.2024.138266.
[17] S. Seok, G. Haikal, J.A. Ramirez, L.N. Lowes, J. Lim, Finite element simulation of bond-zone behavior of pullout test of reinforcement embedded in concrete using concrete damage-plasticity model 2 (CDPM2), Eng. Struct. 221 (2020) 110984. https://doi.org/10.1016/j.engstruct.2020.110984.
[18] M. Afzal, Y. Liu, J.C.P. Cheng, V.J.L. Gan, Reinforced concrete structural design optimization: A critical review, J. Clean. Prod. 260 (2020) 120623. https://doi.org/10.1016/j.jclepro.2020.120623.
[19] C.A. Coello Coello, A.D. Christiansen, F.S. Hern□ndez, A simple genetic algorithm for the design of reinforced concrete beams, Eng. Comput. 13 (1997) 185–196. https://doi.org/10.1007/BF01200046.
[20] V.K. Koumousis, S.J. Arsenis, Genetic Algorithms in Optimal Detailed Design of Reinforced Concrete Members, Comput.-Aided Civ. Infrastruct. Eng. 13 (1998) 43–52. https://doi.org/10.1111/0885-9507.00084.
[21] M. Lepš, M. Šejnoha, New approach to optimization of reinforced concrete beams, Comput. Struct. 81 (2003) 1957–1966. https://doi.org/10.1016/S0045-7949(03)00215-3.
[22] M.Y. Rafiq, C. Southcombe, Genetic algorithms in optimal design and detailing of reinforced concrete biaxial columns supported by a declarative approach for capacity checking, Comput. Struct. 69 (1998) 443–457. https://doi.org/10.1016/S0045-7949(98)00108-4.
[23] K.C. Hover, The influence of water on the performance of concrete, Constr. Build. Mater. 25 (2011) 3003–3013. https://doi.org/10.1016/j.conbuildmat.2011.01.010.
[24] C. Hu, L. Li, Z. Li, Effect of fiber factor on the workability and mechanical properties of polyethylene fiber-reinforced high toughness geopolymers, Ceram. Int. 48 (2022) 10458–10471. https://doi.org/10.1016/j.ceramint.2021.12.254.
[25] K.C. Onyelowe, S. Hanandeh, V. Kamchoom, A.M. Ebid, H. Imran, M.A. Duque Vaca, G.C. Herrera Morales, N. Ulloa, K.P. Arunachalam, Data-driven framework for prediction of mechanical properties of waste glass aggregates concrete, Sci. Rep. 15 (2025) 20902. https://doi.org/10.1038/s41598-025-05229-0.
[26] N.-D. Hoang, A.-D. Pham, Estimating Concrete Workability Based on Slump Test with Least Squares Support Vector Regression, J. Constr. Eng. 2016 (2016) 5089683. https://doi.org/10.1155/2016/5089683.
[27] ACI PRC-211.1; Selecting Proportions for Normal-Density and High-Density Concrete – Guide. American Concrete Institute: Farmington Hills, MI, USA, 2022. https://standards.globalspec.com/std/14537592/prc-211-1 (accessed November 21, 2025).
[28] M. Nematzadeh, M. Naghipour, Compressing fresh concrete technique and the effect of excess water content on physical–mechanical properties of compressed concrete, Mater. Des. 37 (2012) 256–267. https://doi.org/10.1016/j.matdes.2011.12.051.

[29] H.-L. Wang, J.-G. Dai, X.-Y. Sun, X.-L. Zhang, Characteristics of concrete cracks and their influence on chloride penetration, Constr. Build. Mater. 107 (2016) 216–225. https://doi.org/10.1016/j.conbuildmat.2016.01.002.
[30] J. Krassowska, Experimental and analytical study on concrete mechanical properties of recycled carbon fibers from wind turbine blades, Materials 18 (2025) 4105. https://doi.org/10.3390/ma18174105.
[31] ASTM C293/C293M; Standard Test Method for Flexural Strength of Concrete (Using Simple Beam with Center-Point Loading). ASTM International: West Conshohocken, PA, USA, 2016. https://standards.iteh.ai/catalog/standards/astm/b9f82370-8962-477e-ad24-7dba181ae888/astm-c293-c293m-16 (accessed July 23, 2025).
[32] W. Sun, T. Gao, J. Zhao, H. Cheng, Research on fracture behavior and reinforcement mechanism of fiber-reinforced locally layered backfill: experiments and models, Constr. Build. Mater. 366 (2023) 130186. https://doi.org/10.1016/j.conbuildmat.2022.130186.
[33] X. Ren, Y. Xie, F. Ding, D. Sun, H. Liu, Steel fiber reinforced concrete: a systematic review of usage in shield tunnel segment, Sustainability 16 (2024) 10832. https://doi.org/10.3390/su162410832.
[34] L. Zhou, Y. Yu, Y. Zheng, Y. Ye, Y. Wang, J. Lao, Investigation on bond behavior of GFRP bar embedded in ultra-high performance polyoxymethylene fiber reinforced concrete, Eng. Struct. 324 (2025) 119324. https://doi.org/10.1016/j.engstruct.2024.119324.
[35] X. Zhang, Q. Lu, Y. Wang, Experimental Study on Bond Behavior between Steel Rebar and PVA Fiber-Reinforced Concrete, Coatings 13 (2023) 740. https://doi.org/10.3390/coatings13040740.
[36] Fishstone, “PVA Fibers datasheet.” Accessed: Mar. 19, 2025. [Online]. Available: https://concretecountertopsupply. com/pva-fibers/, (March.19). https://concretecountertopsupply.com/pva-fibers/ (accessed March 19, 2025).
[37] PINKBAR®+ Fiberglas™ Rebar | Owens Corning Composites. https://www.owenscorning.com/en/composites/product/pinkbar-plus-fiberglass-rebar (accessed March 19, 2025).
[38] M.L. Manfaluthy, J.J. Ekaputri, The Application of PVA Fiber to Improve the Mechanical Properties of Geopolymer Concrete, MATEC Web Conf. 138 (2017) 01020. https://doi.org/10.1051/matecconf/201713801020.
[39] R. Diao, Y. Cao, M.M. Michel, A. Wang, L. Sun, F. Yang, Mechanical performance study of PVA fiber-reinforced seawater and sea sand cement-based composite materials, Sci. Rep. 14 (2024) 18161. https://doi.org/10.1038/s41598-024-65000-9.
[40] K. Brózda, J. Selejdak, P. Koteš, ANALYSIS OF PROPERTIES OF THE FRP REBAR TO CONCRETE STRUCTURES, 2 (2017).
[41] M. Orouji, E. Najaf, Effect of GFRP rebars and polypropylene fibers on flexural strength in high-performance concrete beams with glass powder and microsilica, Case Stud. Constr. Mater. 18 (2023) e01769. https://doi.org/10.1016/j.cscm.2022.e01769.
[42] B. Benmokrane, B. Zhang, A. Chennouf, Tensile properties and pullout behaviour of AFRP and CFRP rods for grouted anchor applications, Constr. Build. Mater. 14 (2000) 157–170. https://doi.org/10.1016/S0950-0618(00)00017-9.
[43] M. Smolnicki, G. Lesiuk, P. Stabla, B. Pedrosa, S. Duda, P. Zielonka, C.C.C. Lopes, Investigation of flexural behaviour of composite rebars for concrete reinforcement with experimental, numerical and machine learning approaches, Philos. Trans. R. Soc. Math. Phys. Eng. Sci. 381 (2023) 20220394. https://doi.org/10.1098/rsta.2022.0394.
[44] M. Hassan, B. Benmokrane, A. ElSafty, A. Fam, Bond durability of basalt-fiber-reinforced-polymer (BFRP) bars embedded in concrete in aggressive environments, Compos. Part B Eng. 106 (2016) 262–272. https://doi.org/10.1016/j.compositesb.2016.09.039.
[45] S.K. Padmarajaiah, A. Ramaswamy, A finite element assessment of flexural strength of prestressed concrete beams with fiber reinforcement, Cem. Concr. Compos. 24 (2002) 229–241. https://doi.org/10.1016/S0958-9465(01)00040-3.
[46] R.A. Hawileh, H.A. Musto, J.A. Abdalla, M.Z. Naser, Finite element modeling of reinforced concrete beams externally strengthened in flexure with side-bonded FRP laminates, Compos. Part B Eng. 173 (2019) 106952. https://doi.org/10.1016/j.compositesb.2019.106952.
[47] M. Robert, B. Benmokrane, Effect of aging on bond of GFRP bars embedded in concrete, Cem. Concr. Compos. 32 (2010) 461–467. https://doi.org/10.1016/j.cemconcomp.2010.02.010.

[48] 'Carbon Steel Rebar online', Steel Supply LP. Accessed: Nov. 24, 2025. [Online]. Available: https://www.steelsupplylp.com/structural-steel/steel-supply-store/rebar/rebar-carbon-steel. https://www.steelsupplylp.com/structural-steel/steel-supply-store/rebar/rebar-carbon-steel (accessed December 1, 2025).
[49] 'Carbon Fiber Rebar: Strength, Cost & Applications in 2025'. Accessed: Nov. 24, 2025. [Online]. Available: https://www.gtofrp.com/The-Future-of-Carbon-Fiber-Rebar-High-Modulus-Lightweight-Reinforcement-for-Modern-Construction-id46006306.html. https://www.gtofrp.com/The-Future-of-Carbon-Fiber-Rebar-High-Modulus-Lightweight-Reinforcement-for-Modern-Construction-id46006306.html (accessed December 1, 2025).
[50] 'CSE519 - FRP Rebar | PDF | Reinforced Concrete | Fibre Reinforced Plastic', Scribd. Accessed: Nov. 24, 2025. [Online]. Available: https://www.scribd.com/document/636936054/CSE519-FRP-rebar, (. https://www.scribd.com/document/636936054/CSE519-FRP-rebar (accessed September 3, 2025).
[51] 'FRP Pricing Page', Made-in-China.com. Accessed: Nov. 24, 2025. [Online]. Available: https://jxsncr.en.made-in-china.com/product/AwqaZFVGAyrn/China-Basalt-Fiber-Rod-Epoxy-Resin-Carbon-Fiber-Rod-Basalt-Fiber-Rebar-Bfrp.html, Made--Chinacom. https://jxsncr.en.made-in-china.com/product/AwqaZFVGAyrn/China-Basalt-Fiber-Rod-Epoxy-Resin-Carbon-Fiber-Rod-Basalt-Fiber-Rebar-Bfrp.html (accessed September 3, 2025).
[52] PVA Fibers. https://concretecountertopsupply.com/pva-fibers/ (accessed March 19, 2025).
[53] Jeong-Hoon Choi and Roger H. L. Chen, Design of continuously reinforced concrete pavements using glass fiber reinforced polymer rebars, (2005).
[54] M. Raifman Atkins, J.,. Johnson, C.,.&. PI, J.G., Vehicle weight safety study academic report, (2024).
[55] AASHTO LRFD Bridge Design Specifications, 9th Edition;American Association of State Highway and Transportation Officials (AASHTO): Washington, DC, USA, 2020. https://www.slideshare.net/slideshow/aashto-lrfd-bridge-design-specifications-9th-editionpdf/259706621 (accessed September 22, 2025).

9. Acknowledgements

The authors express their gratitude for funding for this study from the U.S. Department of Transportation - Transportation Infrastructure Precast Innovation Center (TRANS-IPIC) through Award Number PU-23-RP-05 Phase I & II. The findings and opinions expressed in this article are those of the authors only and do not necessarily reflect the views of the sponsor.

10. Appendices

<u>Journal publications:</u>

1. Duan, J., Yan, H., Tao, C.*, Wang, X., Guan, S., & Zhang, Y. (2025). Integration of Finite Element Analysis and Machine Learning for Assessing Spatial-Temporal Conditions of Reinforced Concrete. Buildings, 15(3), 435.
2. Xiong, X., & Tao, C.* (2025). Utilization of Dredged Sediments from Southern Lake Michigan in Cement Mortar Production. Construction and Building Materials, 494, 143444.
3. Wang, S., Lin, Y., Duan, J., Yan, H., Wang, X., Xiong, X., Huang, Y., Guan, S., & Tao, C.* (2025). Reinforcement Response Prediction of Composite-Concrete Beams using Crack Patterns and Deep learning. Computer-Aided Civil and Infrastructure Engineering, 1-18.

<u>Journal papers under review:</u>

1. Duan, J., Yan, H., Lin, Y., Guan, S., Tao, C. * (submitted in September, 2025). Advanced Structural Health Monitoring and Situational Awareness of Reinforced Concrete Beam using Smart, Self-sensing Composite Reinforcement through Digital Twin Model. Journal of Civil Structural Health Monitoring.

2. Wang, S., Wang, X., Duan, J., Yan, H., Huang, Y., & Tao, C.*. (submitted in August, 2025). UNet-based Buckling Deformation Reconstruction from Strain Distributions and Knowledge Distillation. Engineering Applications of Artificial Intelligence.
3. Duan, J., Wang, X., Yan, H., Wang, S., Huang, Y., & Tao, C.*(submitted in August, 2025). A Damage-informed Digital Twin Framework for Self-sensing Cured-in-place Underground Pipelines. Engineering Structures.
4. Lin, Y., Yan, H., Duan, J., Li, Y., Xiong, X., Guan, S., & Tao, C. (submitted in December, 2025). Multi-objective Metaheuristic Optimization of Reinforced Concrete Beam for Improved Flexural Performance, Transportation Research Record

Presentations:

1. Tao, C., Duan, J., Lin, Y., & Yan, H., Wang, S., Xiong, X., & Guan, S., Data-Driven Smart Composite Reinforcement for Precast Concrete, U.S. Department of Transportation (USDOT) - University Transportation Center (UTC), Transportation Infrastructure Precast Innovation Center (TRANS-IPIC) Workshop, April 22-23, 2025.
2. Tao, C., Data-Driven Smart Composite Reinforcement for Precast Concrete, Transportation Infrastructure Precast Innovation Center (TRANS-IPIC) Monthly Research Webinar, March 28, 2025.
3. Tao, C., Guan, S., & Duan, J., Data-Driven Smart Composite Reinforcement for Precast Concrete, Transportation Infrastructure Precast Innovation Center (TRANS-IPIC) Monthly Research Webinar, September 23, 2024.
4. Tao, C., Guan, S, Duan, J., Lin, Y., & Yan, H. (2024). Data-Driven Smart Composite Reinforcement for Precast Concrete, U.S. Department of Transportation (USDOT) - University Transportation Center (UTC), Transportation Infrastructure Precast Innovation Center (TRANS-IPIC) Workshop, Chicago, IL, April 22, 2024.

Conference paper and presentation:

1. Lin, Y., Yan, H., Duan, J., Li, Y., Xiong, X., Guan, S., & Tao, C.*(accepted). Multi-objective Metaheuristic Optimization of Reinforced Concrete Beam for Improved Flexural Performance. the 105th Transportation Research Board (TRB) Annual Meeting, Washington, D.C., January 11-15, 2026.
2. Tao, C., Guan, S., Duan, J., Lin, Y., Yan, H., Li, Y., Xiong, X. (accepted). Smart Composite Reinforced Concrete System with Digital Twin-Based Monitoring and AI-Driven Condition Assessment. American Concrete Institute Concrete Convention, Chicago, IL, March 29–April 1, 2026.